

Inelastic low-energy collisions of electrons with HeH^+ : rovibrational excitation and dissociative recombination

Roman Čurík*

*J. Heyrovský Institute of Physical Chemistry,
Academy of Sciences of the Czech Republic, v.v.i.,
Dolejškova 3, 182 23 Prague 8, Czech Republic*

Chris H. Greene

Department of Physics and Astronomy, Purdue University, West Lafayette, Indiana 47907, USA

(Dated: August 30, 2018)

Inelastic low-energy (0–1 eV) collisions of electrons with HeH^+ cations are treated theoretically, with a focus on the rovibrational excitation and dissociative recombination (DR) channels. In an application of *ab initio* multichannel quantum defect theory (MQDT), the description of both processes is based on the Born-Oppenheimer quantum defects. The quantum defects were determined using the R-matrix approach in two different frames of reference: the center-of-charge and the center-of-mass frames. The results obtained in the two reference systems, after implementing the Fano-Jungen style rovibrational frame-transformation technique, shows differences in the rate of convergence for these two different frames of reference. We find good agreement with the available theoretically predicted rotationally inelastic thermal rate coefficients. Our computed DR rate also agrees well with available experimental results. Moreover, several computational experiments shed light on the role of rotational and vibrational excitations in the indirect DR mechanism that governs the low energy HeH^+ dissociation process. While the rotational excitation is several orders of magnitude more probable process at the studied collision energies, the closed-channel resonances described by the high- n , rotationally excited neutral molecules of HeH contribute very little to the dissociation probability. But the situation is very different for resonances defined by the high- n , vibrationally excited HeH molecules, which are found to dissociate with approximately 90% probability.

* roman.curik@jh-inst.cas.cz

I. INTRODUCTION

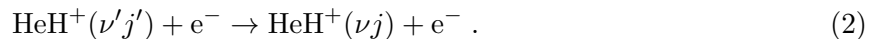
Low-energy collisions of electrons with HeH^+ form one of the many ingredients necessary to understand the chemistry of the early universe [1]. Furthermore, the relative simplicity of the system helps to gauge new experimental setups while also serving as a benchmark for different theoretical models. For these reasons, the low-energy collision process between electrons and the HeH^+ cations has attracted experimental interest [2–9] and theoretical studies [3, 10–15] over the past three decades.

The dissociative recombination (DR) of HeH^+



belongs to a class of processes for which no curve crossing of the target cation and the dissociating neutral exist. The resulting indirect mechanism often led to underestimates of the DR rates in early theoretical studies [1]. It was established later [10, 13, 16, 17] that the light diatomic cations do not always require the presence of a curve crossing to produce a high DR cross section. Multi-channel quantum defect theory (MQDT) helped to understand that the indirect DR is driven by transitions to auto-ionizing Rydberg states attached to a rovibrationally excited ionization threshold. The nuclear dynamics is then driven by non-adiabatic coupling among these Rydberg states. The cross section exhibits series of sharp peaks that accumulate at the rovibrational thresholds. The corresponding auto-ionizing Rydberg states are also referred to in the literature as rovibrational Feshbach resonances.

The second inelastic process that is energetically allowed at very low energies is rovibrational excitation by electron impact



Measurement of the rovibrationally inelastic cross sections is a challenging experimental task, owing largely to the required high electron energy resolution. On the other hand, these cross sections constitute a key ingredient of models designed to determine the initial state populations of the cations in storage rings [18, 19]. While cooling of the target cations in the black body radiation environment should eventually lead to a stable Boltzmann distribution, the additional inelastic collisions with the electrons can modify and establish quite different rovibrational populations of the cations. Despite its importance, there appears to only be a single previous study that reports the rotationally inelastic cross sections for $e^- + \text{HeH}^+$, namely [15].

Several theoretical methods have been applied to treat the non-adiabatic recombination nuclear dynamics in electron collisions with the HeH^+ cation, with various levels of success. Guberman in his pioneering work [10] adopts a traditional description of the non-adiabatic nuclear dynamics. He identifies the discrete-continuum coupling via avoided crossing of the C state (open channel) of the neutral HeH and its D state that lies in the closed-channel space. The coupling between the target cation and the Rydberg series of the neutral is described using quantum defect theory (QDT). Rotational degrees of freedom were not included in the Guberman study and their importance for the dissociative and inelastic processes remains to be investigated.

The theoretical methodology used by Takagi 2004 [12, 14] is closer in spirit to the present approach. Takagi constructed his Born-Oppenheimer wave function at short electronic distances from the fixed-nuclei quantum defects. Following a rovibrational frame transformation (FT), the wave function was expressed in terms of the asymptotic (or channel) quantum numbers. Then the asymptotic boundary conditions were imposed by the usual MQDT closed channel elimination procedure. The main difference from the present study lies in the description of the nuclear continuum. Takagi used real-valued box states that seem to be connected to the asymptotic dissociative states by a simultaneous renormalization of the nuclear and electronic parts of the total wave function. In the second, more recent study, Takagi and Tashiro [14] carried out two different studies that utilized different coordinate system centers. They reported that the DR cross sections computed in the center-of-mass system (CMS) are about two orders of magnitude smaller than the cross section computed in the center-of-charge system (CCS). Since the choice of the coordinate system is important for justifying the validity of various approximations used in the preset MQDT approach, we also address this issue in the present study.

The computational procedure used by Haxton and Greene [13] is quite similar to the present study. The DR results presented here may be considered as a refinement of those published by Haxton and Greene, as most of the parameters defining the calculations were obtained in that study, and extended to some degree in the present treatment. In particular, the partial waves employed here are limited by $l_{max} = 5$, whereas $l_{max} = 3$ was used in the previous calculations. Moreover, the nuclear dynamics is described here on an interval of interatomic distances from 0.2 to 10 a.u., while [13] used the interval from 0.8 to 5.0 a.u. Finally, more notable difference can be found in the choice of vibrational functions. Ref.[13] employed C-normalized complex functions resulting from the exterior complex scaling method [20] that satisfy conventional C-orthogonality relations, while our model uses Siegert pseudo-states as will be described below.

The present study is motivated by ongoing experimental needs (specifically, a need for the inelas-

tic collision rates) and also by a goal to understand and resolve some computational discrepancies among the different theoretical approaches mentioned above. In order to address these points, we have formulated the following goals.

- a. Determination of accurate CMS and CCS quantum defects of HeH^+ as a function of internuclear distance and explanation of the differences between the CMS and CCS approaches
- b. Computation of rovibrationally inelastic rates for the lowest rovibrational transitions
- c. Test the credibility of our model by computing the DR rates and comparing them with the available experimental data
- d. Analysis of the origin of the dominant low-energy DR peaks and discussion of the DR mechanism for electron collisions with the HeH^+ cation

II. QUANTUM DEFECTS

The quantum defect matrices needed for the present study have been computed using the diatomic UK R-matrix package [21] with the R -matrix boundary at $r_0 = 25$ a.u. In this calculation, bound electron orbitals are described by the Slater type basis (STO) of triple-zeta quality (abbreviated as VB2 in Ref.[22]). Our zero-energy quantum defects were determined by matching the R -matrix, evaluated at 10 meV, to the Coulomb functions at distances beyond the boundary radius. The possible energy dependence of the quantum defects is neglected throughout this study. As is mentioned above, Ref.[14] observed that the choice of the coordinate system origin substantially affects the final DR probabilities. In order to address this issue we decided to calculate the two sets of quantum defects. The first set is evaluated in the center-of-charge system (CCS), while the second set of quantum defects is computed in the center-of-mass system (CMS). The comparison of these two approaches is shown in Fig. 1 for the $^2\Sigma$ -symmetry of the Rydberg electron. The blue circles represent s - and p -wave quantum defects of the lithium atom which represents the united atom limit at $R \rightarrow 0$.

The diagonal elements of the μ -matrix shown in the upper panel resemble undulations observed previously for LiHe [23] and for LiH [24]. These oscillatory features in the potential curves arise from the same mechanism that produces ultra-long-range Rydberg molecules, studied extensively in recent years, and can be understood semi-quantitatively using the Fermi zero-range pseudopotential. See, for instance, [25–31]. The quantum eigendefects displayed in lower panel of Fig. 1

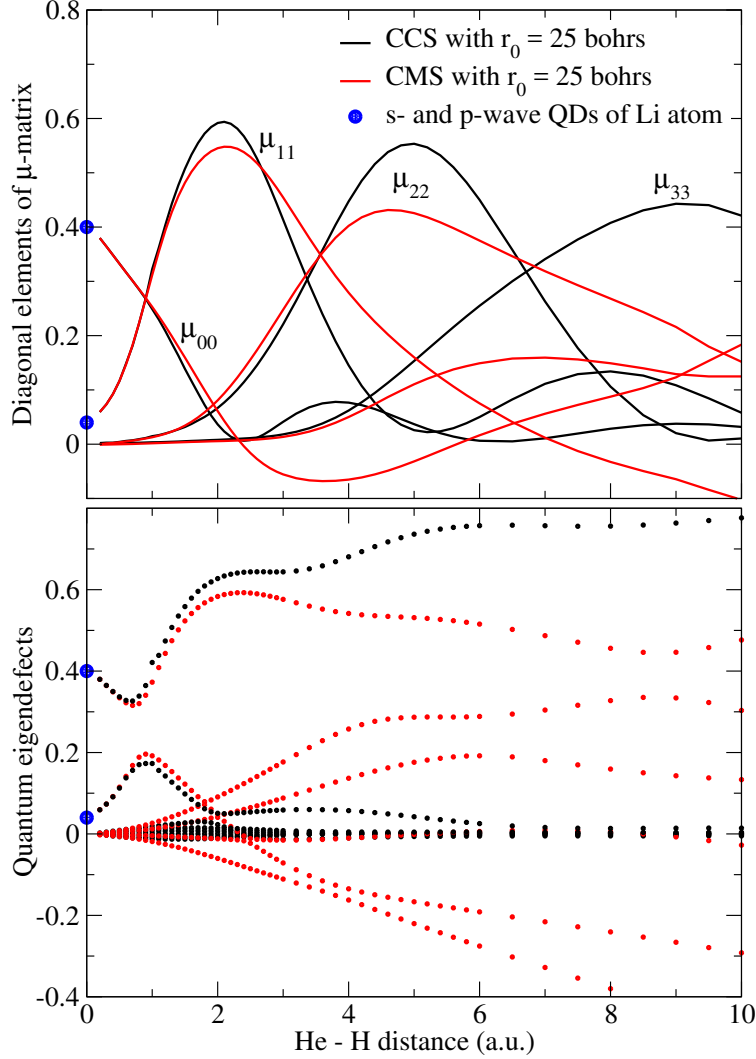


FIG. 1. The elements of the quantum defect matrix μ are shown for $^2\Sigma$ -symmetry of HeH. The upper panel plots the diagonal elements of the μ -matrix while the lower panel displays its eigenvalues. CMS stands for the center-of-mass system while CCS denotes the center-of-charge system.

confirm the observations of Takagi and Tashiro [14] that these two sets of quantum defects differ significantly at larger internuclear distances. On the other hand there is only one set of quantum eigendefects $\mu_\gamma(R)$ that can be obtained by inverting the Rydberg diatomic equation (as developed by Mulliken)

$$U_{n\gamma}(R) = U^+(R) - \frac{1}{2[n - \mu_\gamma(R)]^2}, \quad (3)$$

where $U_{n\gamma}(R)$ is the adiabatic potential energy of the Rydberg states and the potential curve of the cation HeH^+ is denoted as $U^+(R)$. The eigendefects $\mu_\gamma(R)$ are independent of the coordinate system since they can be determined by a difference of the two potential energy curves.

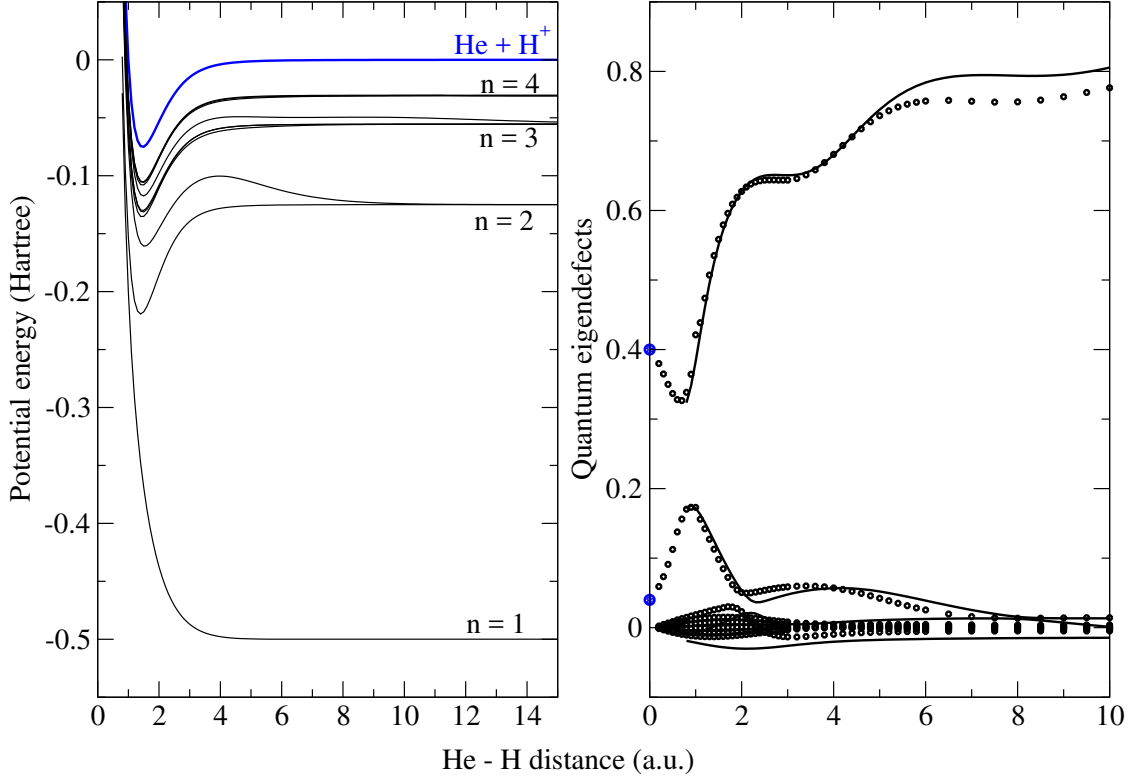


FIG. 2. Left panel: Potential energy curves of HeH in $^2\Sigma$ -symmetry together with the ground cation curve. Right panel: quantum eigendefects extracted from $n = 4$ Rydberg states of the left panel (dots), lines represent the CCS eigendefects already shown in Fig. 1.

Positive energy and negative energy eigendefects approach each other at zero energy by Seaton's theorem [32] and thus our scattering calculations can be cross-checked by comparing with the Rydberg potential energy curves determined from independent quantum chemistry calculations. Such a comparison is shown in Fig. 2, where the left panel shows the ground state cation curve $U^+(R)$ and the series of $^2\Sigma$ -symmetry Rydberg states up to $n=4$. The right panel (full lines) shows the eigendefects $\mu_\gamma(R)$ extracted through Eq. (3). These results demonstrate that the CCS quantum defects give correct Rydberg energies while the CMS quantum defects (see Fig. 1) differ significantly.

In order to clarify the difference between the CCS and CMS quantum defects, the electronic wave function is propagated to the radial distance $r_0=1000$ a.u. and then the quantum defects matrix is determined. In the case of the CCS the asymptotic potential has a form of the Coulomb field and the quantum defects determined at $r_0=1000$ a.u. are identical with those determined at $r_0=25$ a.u. (shown in Fig. 1). However, in the case of the CMS propagation the asymptotic

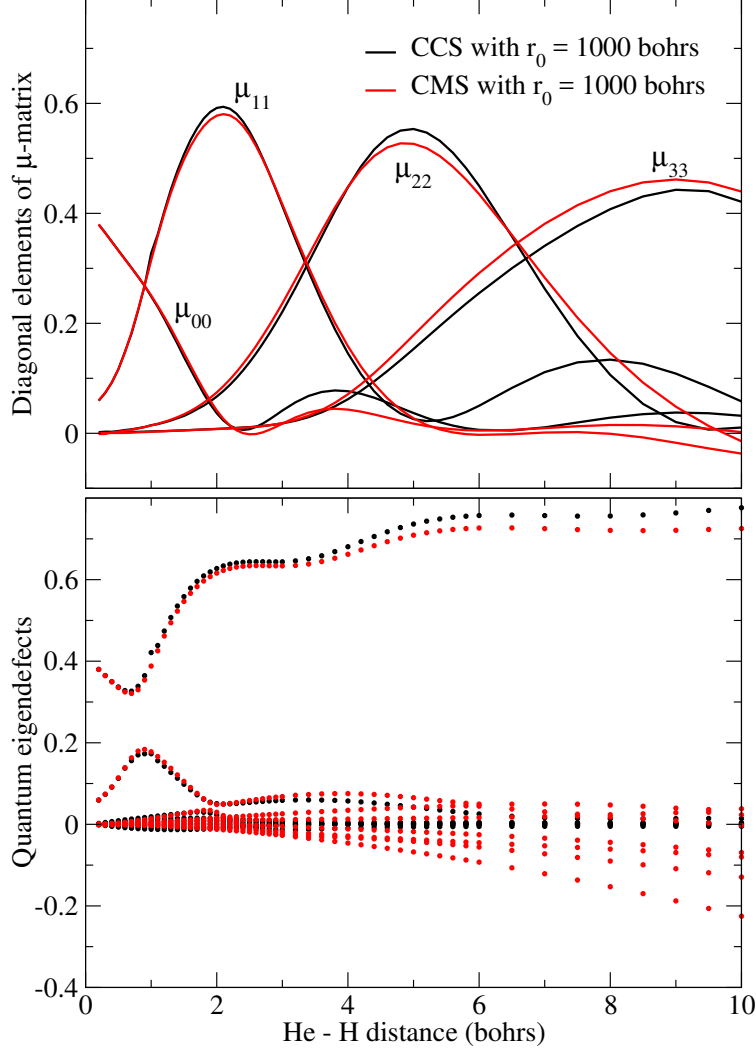


FIG. 3. Same as Fig. 1. Quantum defects were determined by matching at $r_0=1000$ a.u.

potential also contains a dipolar interaction that gives an additional phase (quantum defect) gain together with an enhanced coupling of the partial waves involved. Resulting comparison of the two models (CCS and CMS) propagated to $r_0=1000$ a.u. is shown in Fig. 3. The two sets of quantum defects become very similar. Small differences at larger R can be attributed to the dipole moment coupling of partial waves in the outer region. The angular space presently limited by $l_{max} = 5$ may be insufficient to correctly describe the net phase gain of the lowest partial waves.

To summarize, the only differences among the quantum defects determined at a finite radius r_0 and for different centers of the origin can be attributed to a phase gain in the outer dipole field. This phase gain is missing for those choices of the origin that produce the asymptotic dipole potential. These conclusions constitute a theoretical problem that appears during the frame transformation

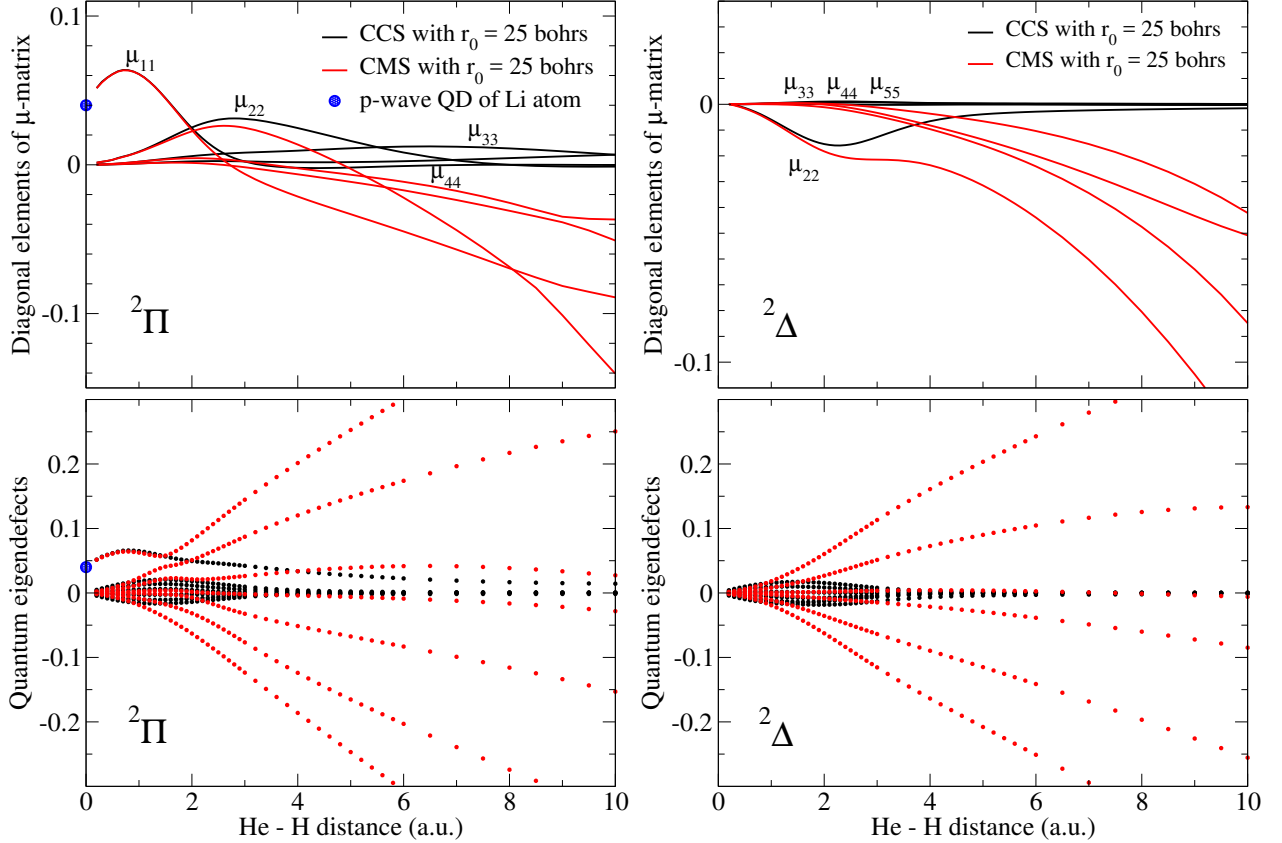


FIG. 4. Elements of the quantum defect matrix μ for $^2\Pi$ (left panel) and $^2\Delta$ (right panel) symmetries of HeH. Upper panels show the diagonal elements of the μ -matrix while the lower panels display their eigenvalues.

technique and it will be discussed later.

For the sake of completeness we also present the quantum defects for $^2\Pi$ and $^2\Delta$ symmetries, as shown in Fig. 4. The missing dipole propagation in the CMS case gives a strong effect because the $^2\Pi$ and $^2\Delta$ quantum defects are smaller when compared to the $^2\Sigma$ symmetry.

III. FRAME TRANSFORMATIONS

The role of the frame transformation (FT) here is to connect the total wave function (electronic and nuclear) in two different electronic spatial volumes. The first (inner) spatial region is defined by the interior of a sphere (of the radius r_0) enclosing the HeH⁺ system. In the second (outer) region where $r \geq r_0$, we assume that the interaction between the electron and the cation is purely Coulombic. In the two spatial regions we use different, but physically appropriate, quantization schemes for the nuclear degrees of freedom. Inside the sphere ($r \leq r_0$) the Born-Oppenheimer ap-

proximation often holds, and the colliding electron moves in the potential of fixed nuclei, whereby the nuclear positions are considered as “good quantum numbers” describing this part of the electron motion. On the other hand the asymptotic channels outside the sphere are defined by the rovibrational states of the cation that are coupled by the electronic part of the wave function expressed by Coulomb functions. Therefore, the radius r_0 should be small enough so the Born-Oppenheimer approximation is accurate inside there sphere. This requirement, when combined with our conclusions on the CMS and CCS quantum defects, represents a dilemma for determining the most appropriate FT distance r_0 :

- a. At $r_0 = 25$ Bohr radii the CMS quantum defects behave wildly (Figs. 1 and 4), they are likely not converged with respect to the number of partial waves and their corresponding eigendefects do not reproduce energies of the bound Rydberg states. On the other hand, the CCS quantum defects diminish quickly with the higher angular momentum l and its projection Λ . They also satisfactorily reproduce the bound state energies via Seaton’s theorem (Fig. 2). However, a direct application of the CCS defects is complicated by physics - the molecule does not rotate around the center of charge. In reality the electron collides with a rotating dipolar cation.
- b. At $r_0 = 1000$ Bohrs the differences between the two sets of quantum defects disappear and the bound state energies are also well reproduced by the CMS quantum defects that are more physical to consider for the rotational FT. An inherent problem with this approach stems from the limited accuracy of the Born-Oppenheimer approximation inside a volume of such large radius.

It is clear that both of the available options bring a certain level of an approximation into the computational model. Corresponding inaccuracies can hardly be estimated beforehand and therefore, we have chosen to carry out the FT for both, CMS and CCS quantum defects, in order to critically compare resulting inelastic and DR rates.

A. Rovibrational states

The rovibrational nuclear states of the HeH^+ cation define the asymptotic electron escape channels and they have the form of [33] (Hund’s case b)

$$\chi_{\nu j}(R, \hat{\mathbf{R}}) = \phi_{\nu j}(R) Y_{jM-m}(\hat{\mathbf{R}}), \quad (4)$$

where $M = m + m_j$ is the projection of the total angular momentum $\mathbf{J} = \mathbf{l} + \mathbf{j}$ in the LAB frame, \mathbf{j} is the angular momentum describing the molecular rotations, \mathbf{l} is the orbital angular momentum of the colliding electron, and ν indexes the molecular vibrational functions. The rovibrational states

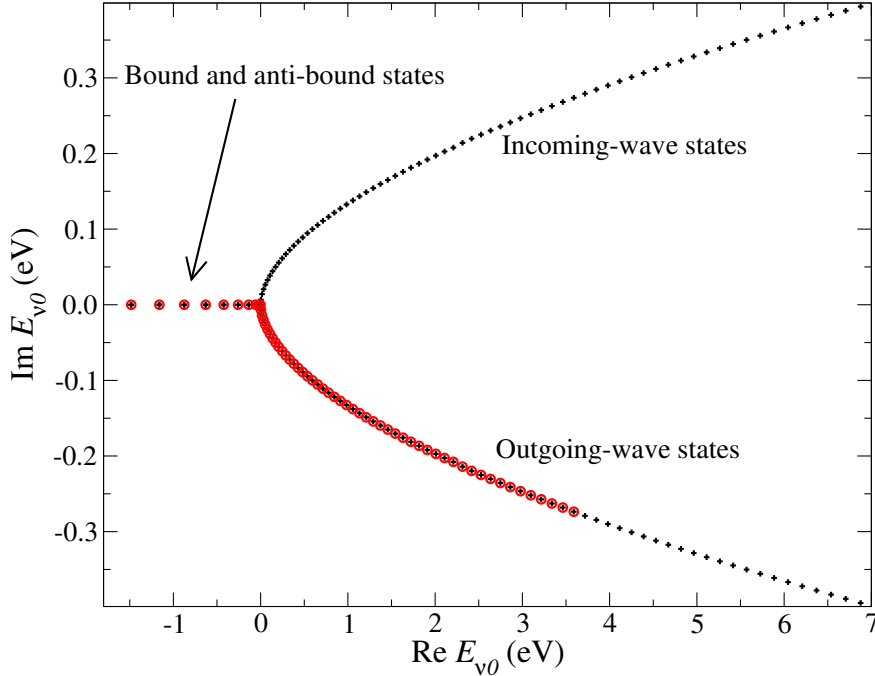


FIG. 5. Distribution of the energy eigenvalues $E_{\nu j} = K_{\nu j}^2/2\mu$ (Eq. 5) in the complex plane for $j = 0$. Circles denote the 60 states used in the present calculations.

$\phi_{\nu j}(R)$ and corresponding energies were obtained by solving nuclear Schrödinger equation

$$\left[-\frac{d^2}{dR^2} + 2M_r U^+(R) + \frac{j(j+1)}{R^2} - K_{\nu j}^2 \right] \phi_{\nu j}(R) = 0, \quad (5)$$

with Siegert [34, 35] boundary conditions at the origin and at $R_0 = 10$ a.u.

$$\phi_{\nu j}(0) = 0; \quad \phi_{\nu j}(r) \sim R h_j^{(1)}(K_{\nu j} R) \text{ for } R \geq R_0, \quad (6)$$

where $h_j^{(1)}$ is the spherical Hankel function of the first kind. In other words, the boundary condition at R_0 selects only those solutions, whose asymptotic momentum $K_{\nu j}$ coincides with the energy eigenvalues $E_{\nu j} = K_{\nu j}^2/2\mu$, leading to a form of continuum discretization as shown in Fig. 5. The circled states denote a subset of 60 Siegert states that resulted in converged results for electron collision energies up to 2.5 eV.

The cation curve $U^+(R)$ employed in Eq. (5) (also shown by the blue line in Fig. 2) was computed by the full CI method using Dunning's aug-cc-pV5Z basis [36] as implemented in Molpro

2012. The reduced mass $M_r = 1467.28$ (for $^4\text{HeH}^+$) was taken from Ref. [37] (denoted as μ_{eff} in Tab. 3). Resulting rovibrational energies are in a very good agreement (within 2 cm^{-1}) with accurate calculations of Pachucki and Komasa 2012 [38] for $\nu \leq 5$ and $j \leq 12$ listed in Tab. III of Ref. [38].

B. Rovibrational frame transformation

We implement the rovibrational FT as a two-step procedure. The first step is the vibrational frame transformation [33, 39], later modified [40] to account for the modified Siegert state orthonormality relation, via

$$S_{l\nu, l'\nu'}^\Lambda(j, j') = \int_0^{R_0} dR \phi_{\nu j}(R) S_{l'l'}^\Lambda(R) \phi_{\nu' j'}(R) + i \frac{\phi_{\nu j}(R_0) S_{l'l'}^\Lambda(R_0) \phi_{\nu' j'}(R_0)}{K_{\nu j} + K_{\nu' j'}}. \quad (7)$$

The second step is accomplished by the rotational frame transformation [33]

$$S_{l\nu j, l'\nu' j'}^{J\eta} = \sum_{\Lambda} U_{j\Lambda}^{J\eta l} S_{l\nu, l'\nu'}^\Lambda(j, j') U_{j'\Lambda}^{J\eta l'}, \quad (8)$$

where $\eta = (-1)^{l+j}$ is the total parity of the neutral system. It is worth to note that in the present dissociative recombination results the contribution of the odd parity cross section is negligible (less than 0.5%) because only $\Lambda > 0$ contributes to the $\eta = -1$ symmetry [33] and the small $^2\Pi$ and $^2\Delta$ quantum defects, shown in Fig. 4, seem to have a weak impact on the dissociation dynamics.

Due to the Coulomb nature of the asymptotic potential, the matrix $S_{l\nu j, l'\nu' j'}^{J\eta}$ exhibit only a very weak energy dependence, which is completely neglected in the present study. Moreover, it cannot be regarded as the inelastic S -matrix of the scattering theory as it represents merely a set of coefficients coupling rovibrational channels with the electronic wave functions for which the physical asymptotic boundary conditions have not yet been applied, namely in the closed channels. The application of the electronic boundary conditions in the MQDT closed-channel elimination step leads to the physically relevant S -matrix, which of course is defined only in the open-channel space [41]

$$\mathbf{S}^{\text{phys}} = \mathbf{S}^{oo} - \mathbf{S}^{oc} \left[\mathbf{S}^{cc} - e^{-2i\beta(E)} \right]^{-1} \mathbf{S}^{co}, \quad (9)$$

where the superscripts o and c denote open and closed sub-blocks in the unphysical S -matrix $S_{l\nu j, l'\nu' j'}^{J\eta}$, respectively. The diagonal matrix $\beta(E)$ describes effective Rydberg quantum numbers with respect to the close-channel thresholds:

$$\beta_{ij} = \frac{\pi}{\sqrt{2(E_i - E)}} \delta_{ij}. \quad (10)$$

IV. ROVIBRATIONAL EXCITATION

The rovibrationally inelastic cross section is computed from the physical S -matrix $S_{l\nu j, l'\nu' j'}^{\text{phys}, J\eta}$ as [33, 42]

$$\sigma_{(\nu' j') \rightarrow (\nu j)}(\varepsilon_{\nu' j'}) = \frac{\pi}{2\varepsilon_{\nu' j'}(2j' + 1)} \sum_{J\eta l l'} (2J + 1) \left| T_{l\nu j, l'\nu' j'}^{J\eta} \right|^2, \quad (11)$$

where $\varepsilon_{\nu' j'} = E - E_{\nu' j'}$ is the incident electron collision energy and the state-to-state scattering amplitudes $T_{l\nu j, l'\nu' j'}^{J\eta}$ are defined by

$$T_{l\nu j, l'\nu' j'}^{J\eta} = S_{l\nu j, l'\nu' j'}^{\text{phys}, J\eta} - \delta_{ll'} \delta_{\nu\nu'} \delta_{jj'}. \quad (12)$$

The corresponding inelastic rate coefficient $\alpha(\varepsilon)$ is obtained by multiplying the cross section by velocity, and thermally averaging it when necessary:

$$\alpha(\varepsilon) = \sqrt{2\varepsilon} \sigma(\varepsilon). \quad (13)$$

The discussion of our results begins with a comparison of the rotational excitation rates of the HeH^+ cation computed in the center-of-mass and center-of-charge systems. Both rates are shown in the left panel of Fig. 6. It is not surprising that the non-zero dipole moment in the center-of-mass system visibly influences the $0 \rightarrow 1$ and $0 \rightarrow 3$ transitions. The transition $0 \rightarrow 4$ is also strongly impacted by the choice of the frame of reference (or a distance r_0 at which the rotational FT is carried out), however, the cross sections are already quite low.

The present center-of-mass results are also compared to recent calculations of Hamilton *et al* 2016 [15], as displayed in the right panel of Fig. 6. Aside from the $0 \rightarrow 1$ transition, the remaining results of Hamilton *et al* 2016 strongly resemble the present CCS results (and the same as the CMS results with the electronic calculation performed out to a large radius, $r_0 = 1000$ a.u.). This similarity can be explained by the differences in the two theoretical models used to compute the inelastic rates:

- (i) In the present calculations the scattered electron is described at the sphere with $r_0 = 25$ a.u. with partial waves $l \leq 5$. While the rotational FT at this distance is quite accurate, the present CMS results neglect the external dipole field for $r > r_0$.
- (ii) In the calculations of Hamilton *et al* 2016 [15] the R-matrix radius is chosen at $r_0 = 13$ Bohr radii and the partial wave expansion is limited by $l \leq 4$. However, the LAB frame propagation for $r > r_0$ is accounted for by the Coulomb-Born closure technique [43] that is

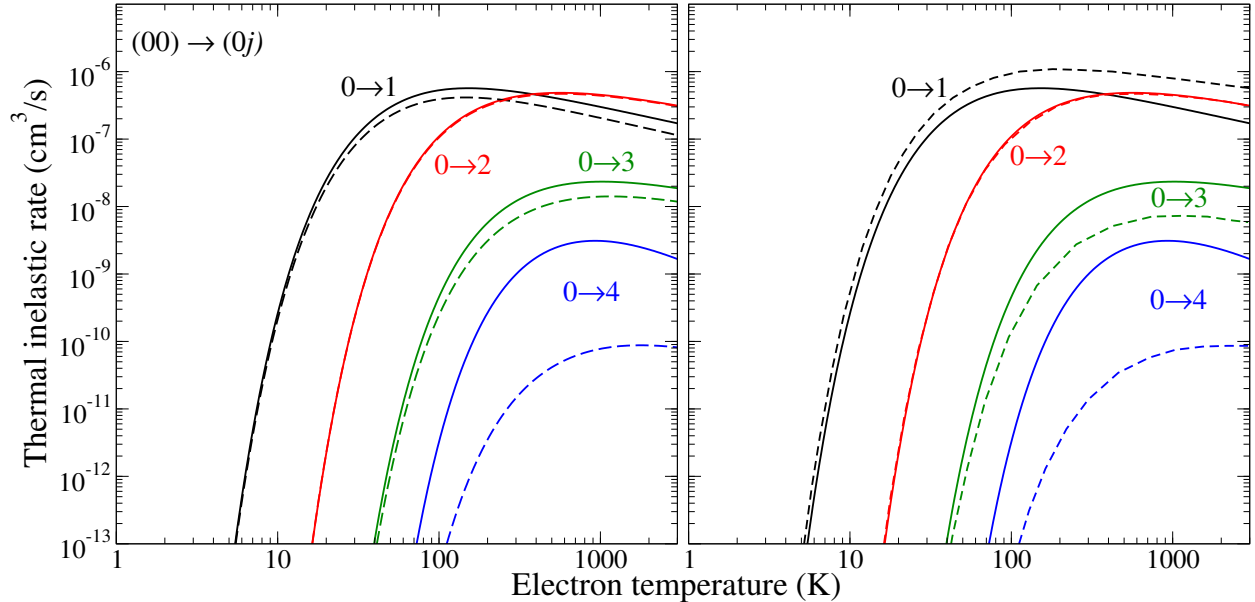


FIG. 6. Thermal rates of rotational excitation of HeH^+ from the rovibrational ground state $(\nu j) = (00)$. The left panel shows comparison of the present center-of-mass (full curves) and center-of-charge (broken curves) results. The right panel compares the present center-of-mass results with recent CMS calculations of Hamilton *et al* 2016 [15]. Note that in both panels the broken and full curves overlap for the $0 \rightarrow 2$ excitations.

designed to add, incoherently, the missing cross-section contribution associated with higher partial waves in the LAB frame domain. Such procedure is dominant for the $\Delta j = \pm 1$ transitions and it can also be viewed as effectively moving the frame transformation radius r_0 to infinity. This can explain the good agreement with the present center of mass results with FT at $r_0 = 1000$ Bohrs, aside from the $0 \rightarrow 1$ transition. For this transition it is difficult to decide which of the two theoretical models is more accurate.

The data displayed in Fig. 6 are a result of a thermal Boltzmann convolution (see for example [44]) of the energy-dependent inelastic rates. Such rates are shown in Fig. 7 for the four lowest rovibrational initial states. Observe that all the data presented in Fig. 7 share the importance of the two dominant transitions $\Delta j = \pm 1$ and $\Delta j = \pm 2$.

V. DISSOCIATIVE RECOMBINATION

The physical S -matrix (9) is the result of the “closed-channel elimination” technique of MQDT that applies proper electronic boundary condition in the closed channels, i.e. exponentially decaying behavior for the components of the electronic wave function in the closed channels. The present

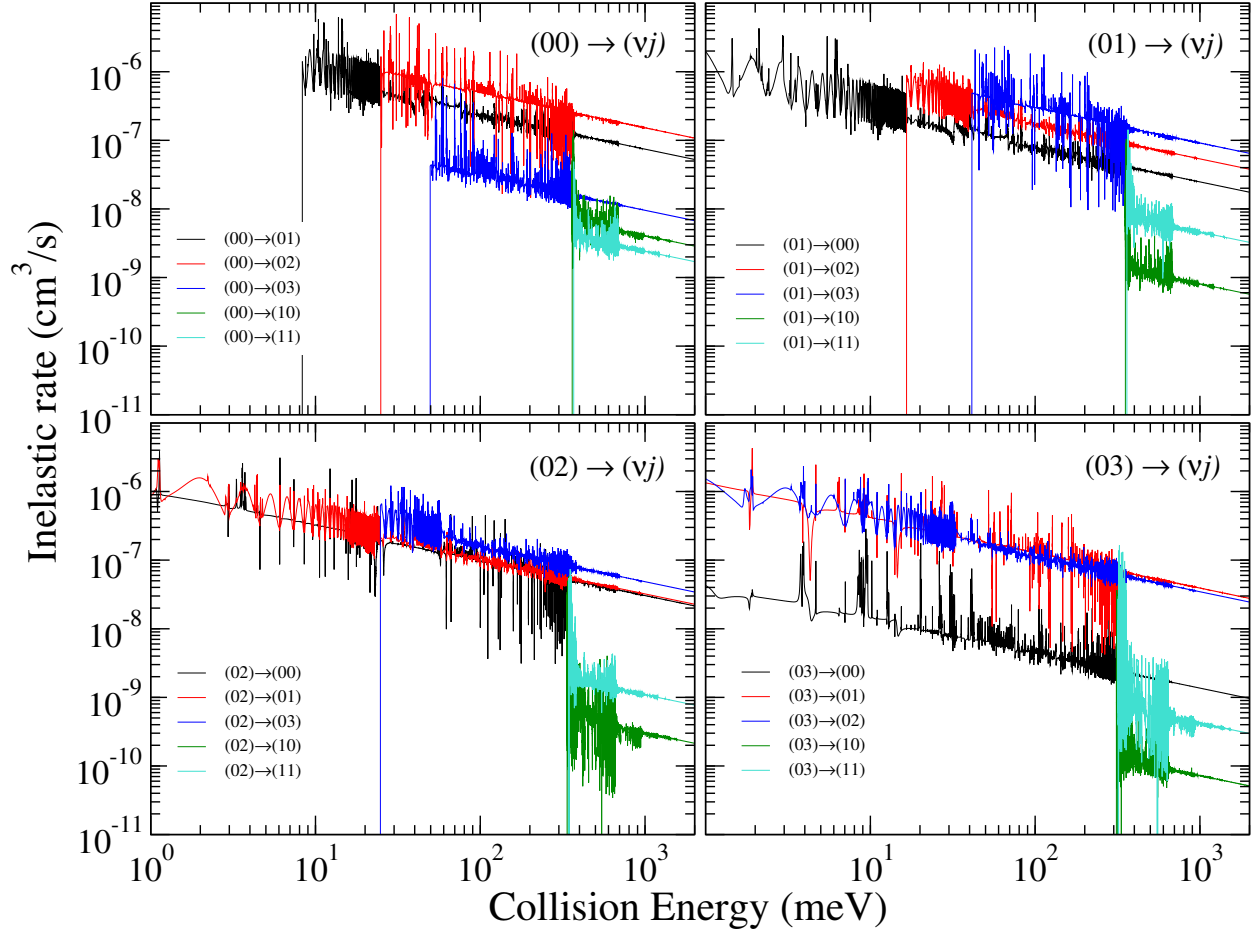


FIG. 7. Computed rates for the inelastic rovibrational transitions of HeH^+ , starting from the initial vibrational ground state $\nu' = 0$.

formulation does not present this wave function in a form that would also enforce proper nuclear boundary conditions in order to obtain the full scattering matrix that includes explicit atom-atom or ion-pair dissociation channels that would yield the DR cross section directly, as was done in the previous theoretical studies [10, 14]. Instead, we use the fact that the electronic S -matrix (9) in the nuclear basis of the complex outgoing-wave Siegert states is subunitary. Following the original idea of Hamilton and Greene 2002 [40], we identify the resulting loss of electronic flux with the only physical mechanism (in the Hamiltonian utilized which omits the radiation field coupling) that can lead to the loss of electrons, namely the dissociative recombination events. This physical idea leads to a mathematical expression for the DR cross section as a function of the incident energy $\varepsilon_{\nu'j'}$ for

the target ion in an initial state defined by $(\nu'j')$:

$$\sigma_{\nu'j'}^{DR}(\varepsilon_{\nu'j'}) = \frac{\pi}{2\varepsilon_{\nu'j'}(2j'+1)} \sum_{J\eta l'} (2J+1) \left(1 - \sum_{l\nu j} S_{l\nu j, l'\nu'j'}^{\text{phys}, J\eta} S_{l'\nu'j', l\nu j}^{+\text{phys}, J\eta} \right). \quad (14)$$

The recombination rate is then connected with the DR cross section using the simple expression (13).

A. Center-of-charge vs. center-of-mass

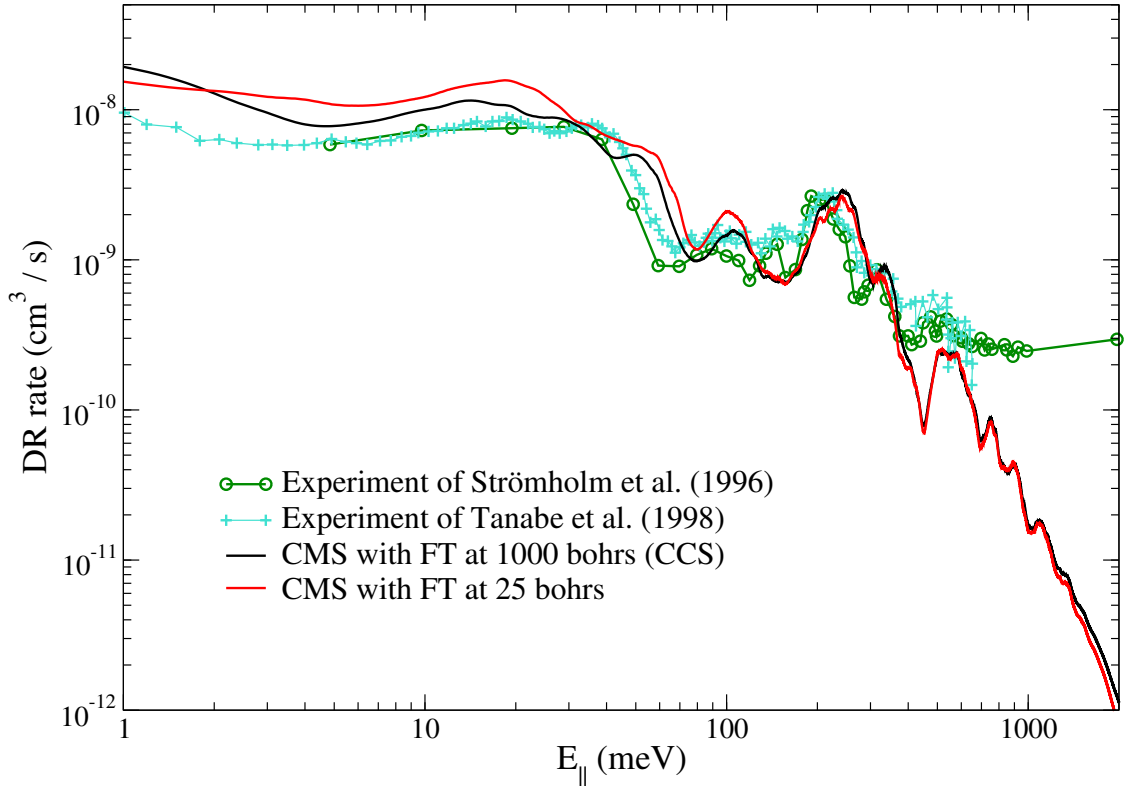


FIG. 8. The DR rates are compared for two calculations with quantum defect matrices determined either in the center-of-charge (CCS) or center-of-mass (CMS) reference systems. The corresponding colors of the quantum defects shown in Figs. 1 and 4 are used. Results are averaged over the Boltzmann population of the cation initial states (at 800K) and over the electron beam energy spread appropriate to a typical current generation storage ring experiment: $\Delta E_{\parallel} = 0.1$ meV and $\Delta E_{\perp} = 10$ meV. The absolute data of Strömholm *et al.* (1996) [7] are displayed as green circles, while the scaled data of Tanabe *et al.* (1998) [9] are shown as turquoise crosses.

The CCS and CMS results are compared in Fig. 8. Our rapidly oscillating results full of dense resonance regions are convolved over the electron beam spreads of $\Delta E_{\parallel} = 0.1$ meV and ΔE_{\perp}

= 10 meV, estimated in the previous experiments [7, 9]. Evidently the difference between the two theoretical approaches is quite small at lower energies (below 100 meV) and it almost disappears at the collision energies above 100 meV. This finding is in clear disagreement (by about 2 orders of magnitude) with the difference demonstrated by Takagi and Tashiro [14] (see Figs. 2 and 3 in the reference). Moreover, the difference between the center-of-mass and the center-of-charge results is so small that the experimental data can hardly help to decide which of the two models is more accurate. We conclude that the center-of-charge results represent the experiments slightly better, and the numerical aspects of our calculations are also under better control in this case (especially the convergence with the number of partial waves included). Therefore, in the following only the center-of-charge DR results are presented.

B. DR for the other isotopologues

The change of the atomic isotopes in the HeH^+ cation has no impact on the electronic part of our CCS calculations that are described in Section II. This change is reflected only in the Siegert states spectrum via modification of the reduced mass M_r in Eq. (5). Since the reduced mass of $^4\text{HeH}^+$ taken from Tab. 3 of Ref. [37] in combination with the presently calculated cation curve resulted in very accurate rovibrational levels, the effective masses listed in Table. 3 of Ref. [37] are also adopted for the other isotopologues. Rovibrational levels calculated with the Siegert equations (5) and (6) yield rovibrational transitions that can be compared with the experimental data (Tab. 6 of Ref. [37]). The agreement is again very good with differences within 1 cm^{-1} for the first four R-lines listed for the each isotopologue. Resulting DR rates are shown in Fig. 9 for all the four isotopologues.

The calculated DR rates generally reproduce the structures seen in the available experiments. The computed data for the other isotopologues share the high-energy deficiency visible already for $^4\text{HeH}^+$ and also in the previous calculations of Haxton and Greene 2009 [13]. This deficiency is represented by lower computed DR rates for higher collision energies (above several hundreds of meV). Such discrepancy can presumably be explained by the so-called "toroidal correction" that is not included in the present study [45]. The toroidal correction accounts for collision events at the edges of the collision area in which the electron and ion beam are merged in the storage rings. The relative collision energies in those edges depend on the velocity vectors of the merging beams. That dependence effectively widens the velocity spreads of the beams and it can also result in an additional background rate brought from the higher-energy collision events.

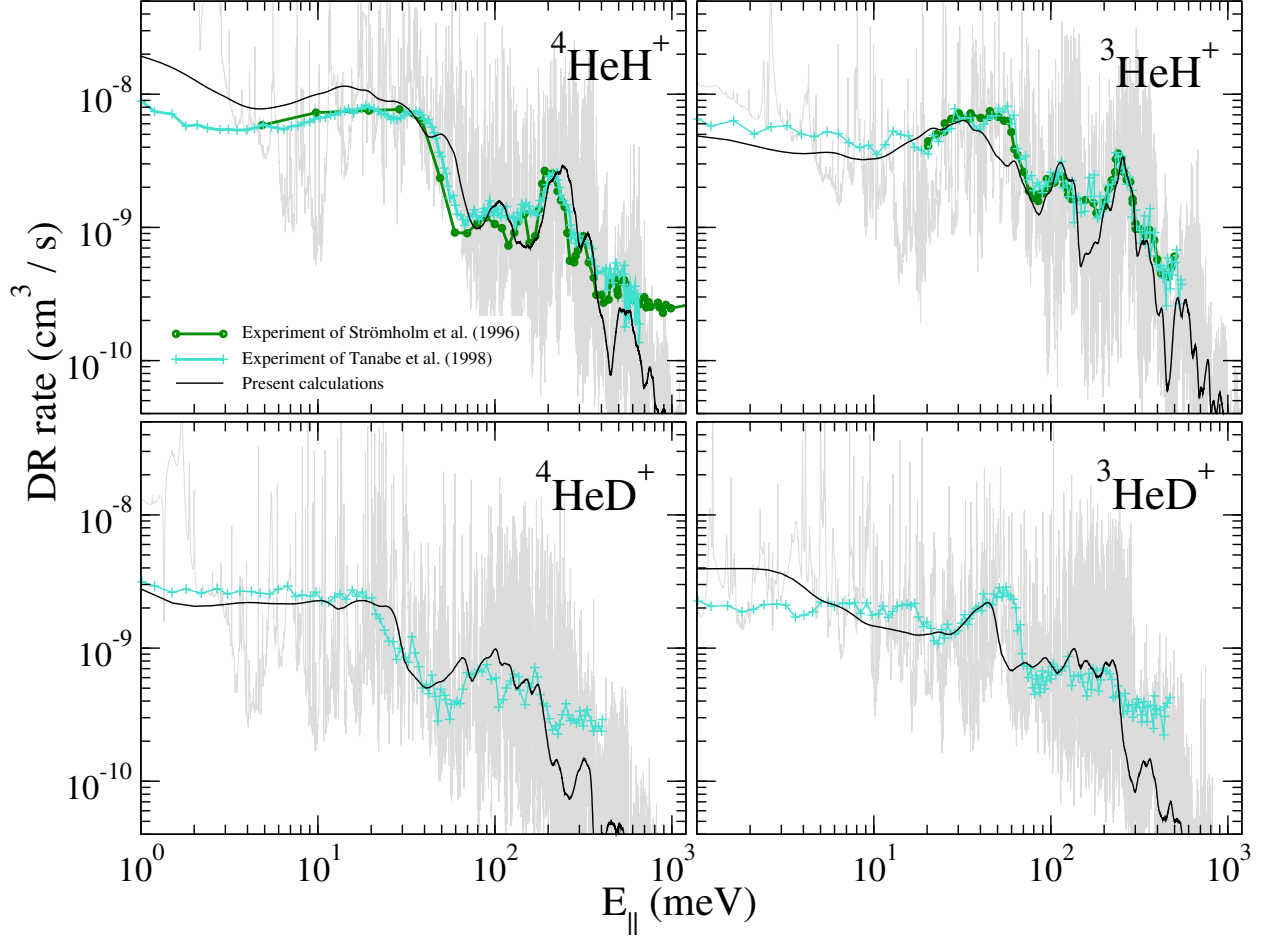


FIG. 9. Computed and measured DR rate for four different isotopologues of HeH^+ cation. Absolute data of Strömholm et al. (1996) [7] are displayed as green circles, while the scaled data of Tanabe et al. (1998) [9] are shown as turquoise crosses. In the upper two panels the data of Tanabe et al. (1998) are scaled to the experiment of Strömholm et al. (1996). In the lower two panels the experiment is scaled arbitrarily to the present calculations shown by the black line. The data in grey represent calculations without the averaging over electron beam energy distributions (Boltzmann population of the initial rovibrational states of $^4\text{HeH}^+$ is still accounted for).

C. Initial state-dependent DR

The results in this section have not been averaged over the initial rovibrational population of the cations. However, the electron beam energy distributions are still averaged over ($\Delta E_{\parallel} = 0.05$ meV and $\Delta E_{\perp} = 1.5$ meV). The beam distribution widths used here are chosen to be smaller than those in the previous section. The reason for this change follows from the fact that there are no experimental data of this type available currently and thus the present data constitute a prediction.

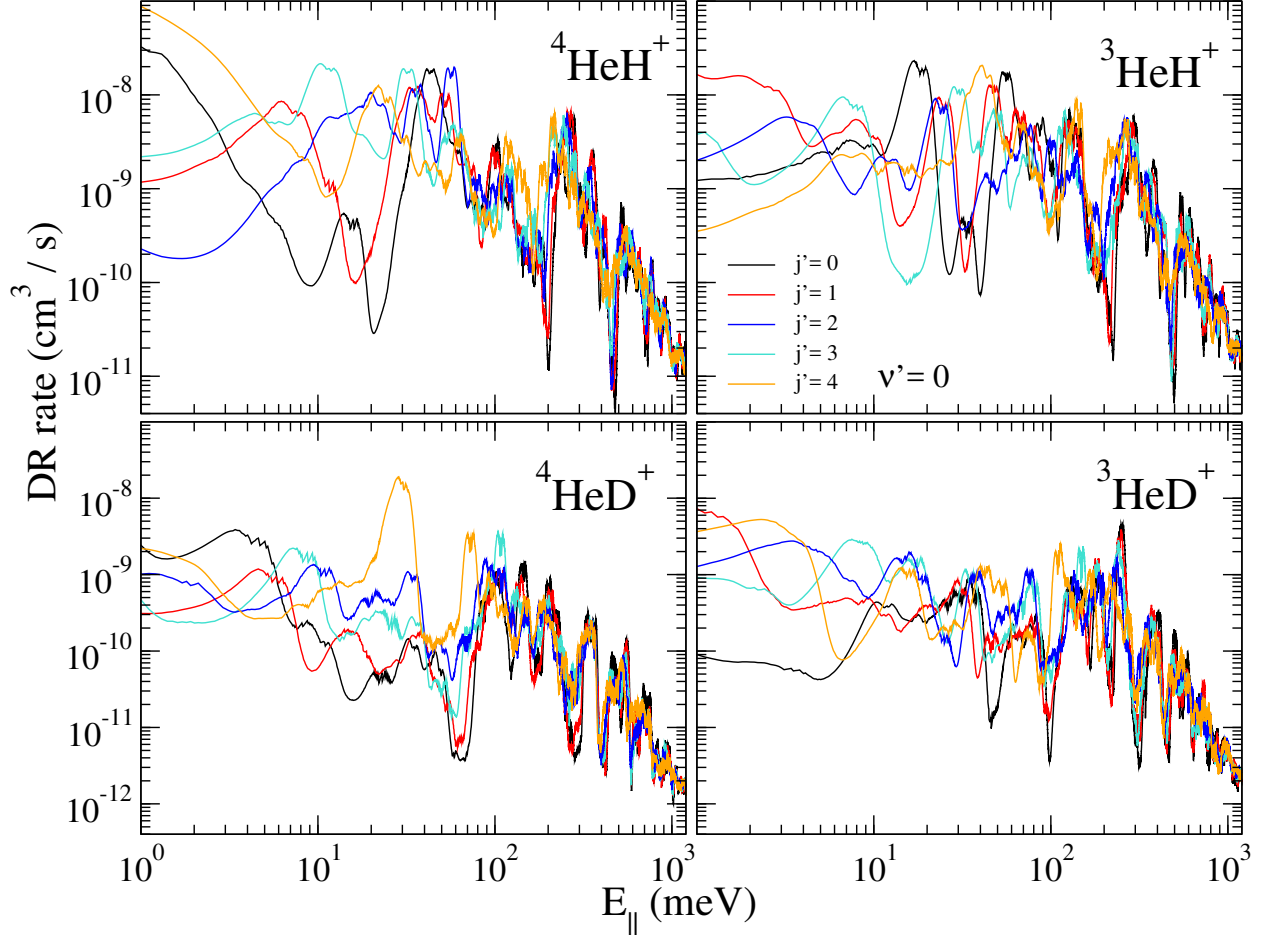


FIG. 10. The computed DR rate is shown for the different initial rovibrational states of the HeH^+ isotopologues, for an initial ground vibrational state $\nu' = 0$. The computed results are convolved over the electron beam energy distributions ($\Delta E_{\parallel} = 0.05$ meV and $\Delta E_{\perp} = 1.5$ meV).

Ideally, such a prediction should be made for the expected experimental conditions, such as for the conditions available in the Cryogenic Storage Ring (CSR) at the Max-Planck Institute for Nuclear Physics [18].

Fig. 10 shows the DR rate for the initial vibrational state $\nu' = 0$ and the lowest rotational states. The $\Delta E_{\perp} = 1.5$ meV is too large to observe any fine structure close to the first rotational thresholds. What is clear, however, is that for the ground initial state $\nu' = 0, j' = 0$, the shape of the DR rate differs significantly when compared with the Boltzmann-averaged results presented in Fig. 9. For example, if the temperature of the cations is in the range of 10–15 K (≈ 1 meV), the population of rotationally excited initial states with $j' > 0$ can be neglected and the DR rate should be dominated by the black curves.

D. First rotational and vibrational thresholds

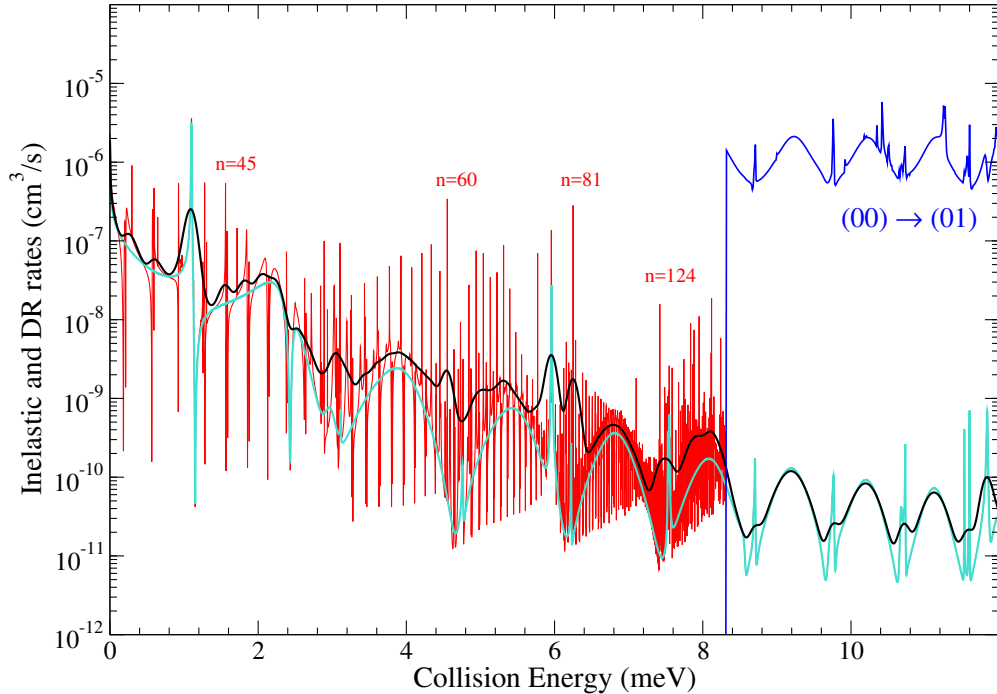


FIG. 11. The computed DR rate from the ground ionic rovibrational state is shown in the vicinity of the first rotational threshold (01). The red line shows the vibrational Feshbach resonances converging to the first rotational threshold. The turquoise curve is unphysical, but serves a useful purpose in our analysis: it was obtained by artificially opening the $j = 1$ channel. Note that the red and turquoise curves coincide above the $j = 1$ threshold. The black curve is a simple one-dimensional convolution of the red-curve data with a Gaussian function (width of 0.1 meV). The blue curve displays the rotationally-inelastic rate for the $(00) \rightarrow (01)$ transition.

Fig. 11 shows the zoomed-in DR rate from the ground rovibrational state near the first inelastic threshold characterized by quantum numbers $\nu = 0$ and $j = 1$. The turquoise curve displays an unphysical DR rate, corresponding to a process in which we forbid the scattering electron to be captured in a Rydberg state while the molecule is rotationally excited to $(\nu, j) = (0, 1)$. Such computational experiments can be easily done by opening artificially the corresponding closed Rydberg channel. The resulting comparison can provide information about the importance of rotations during the DR process. Fig. 11 demonstrates that the enhancement of the DR rate just under the threshold (at ≈ 8 meV) can be estimated to be approximately a factor of 2. On the other hand, the blue curve showing the inelastic rate for the rotational transition $0 \rightarrow 1$ indicates that rotational excitation is a process about 4 orders of magnitude more probable than dissociation.

One can, therefore, conclude that the electrons with these low energies (say under 8 meV) very

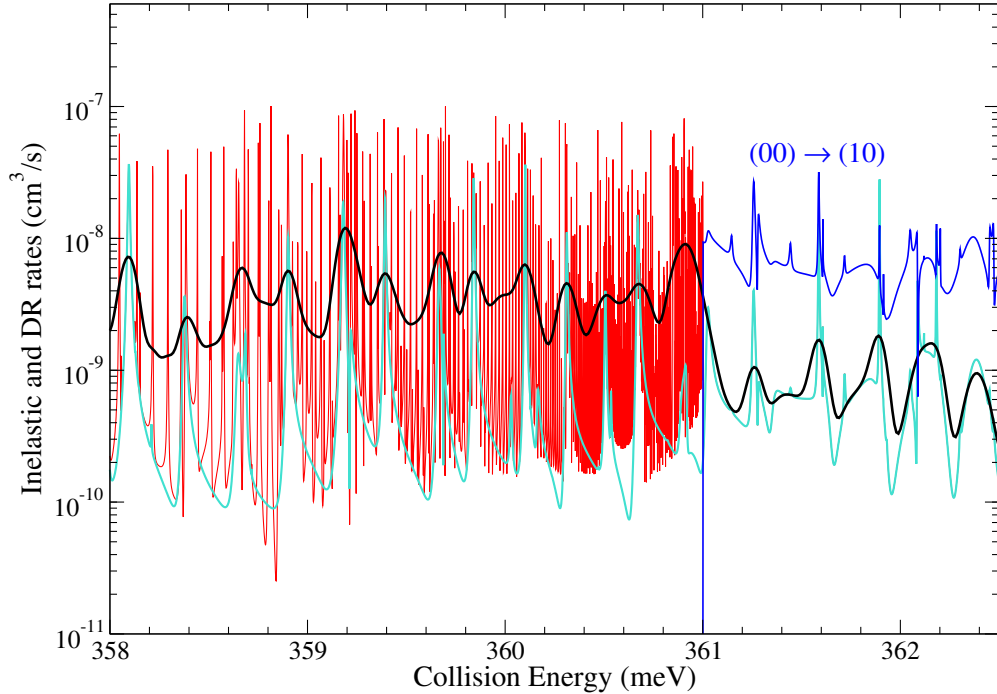


FIG. 12. The DR rate from the ground rovibrational state computed in the vicinity of the first vibrational threshold (10). The coloring scheme is the same as in Fig. 11, except that the blue line displays here the vibrationally inelastic rate for the $(00) \rightarrow (10)$ transition.

efficiently heat the HeH^+ cations rotationally by getting trapped in high Rydberg states (with $n > 40$). However, these temporary, rotationally excited, neutral HeH molecules very rarely dissociate, only about 1 case out of 10,000, probably because the rotational excitation does not excite the molecule along a dissociative coordinate. This hypothesis can be further examined by a near-threshold inspection, similar to the one shown in Fig. 11, but this time around the first vibrational threshold. The corresponding data are displayed in Fig. 12. In contrast to the previous case, closed-channel resonances attached to the first vibrational threshold enhance the DR rate by about one order of magnitude. This enhancement is revealed as the difference between the averaged DR rate (black curve) and the turquoise curve. The enhancement disappears once the collision energy is high enough to open the vibrational excitation channel. Fig. 12 also shows that the DR probability just below the threshold transfers into vibrational excitation probability at energies above the threshold. Stated in more physical language, this also means that about 90% of the temporary, vibrationally excited, neutral high- n HeH molecules that are created by below-threshold collisions of electrons with HeH^+ will dissociate.

This behavior is similar to what was observed in the case of LiH^+ [16] and it may be a universal property of the indirect DR mechanism.

E. More about the DR mechanism

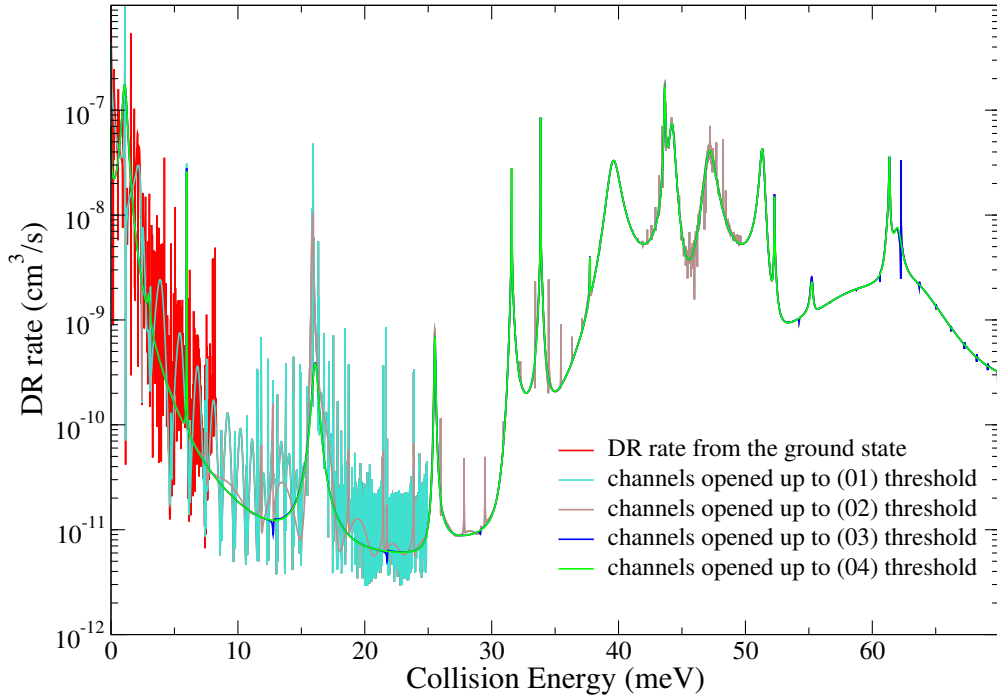


FIG. 13. The computed DR rate from the ground initial state (red curve). The other curves display calculated unphysical data in which all the closed channels are opened up to different rotational thresholds (ν, j) (the thresholds are included in the artificial channel opening procedure). The colors overlap in the listed order. The red curve is at the bottom while the green curve is the top color.

The preceding paragraphs demonstrate that rotational excitation of the HeH^+ during its collisions with an electron play only a minor role in the DR process for energies near the first rotational and vibrational thresholds. In light of this, one might still wonder what is causing the sharp DR enhancements below the first vibrational threshold as can be seen in Fig. 10. As an example we explore the DR rate for $^4\text{HeH}^+$ from the ground rovibrational state (black curve in top left panel in Fig. 10). The computed DR rate, zoomed-in to 0–70 meV, is displayed by the red curve in Fig. 13. This figure is just an energy extension of Fig. 11 calculated at a coarser grid. Fig. 13 also shows results of unphysical calculations in which all the closed channels are artificially opened up to a certain threshold (ν, j) . Only the first four rotational thresholds are opened but we did not observe

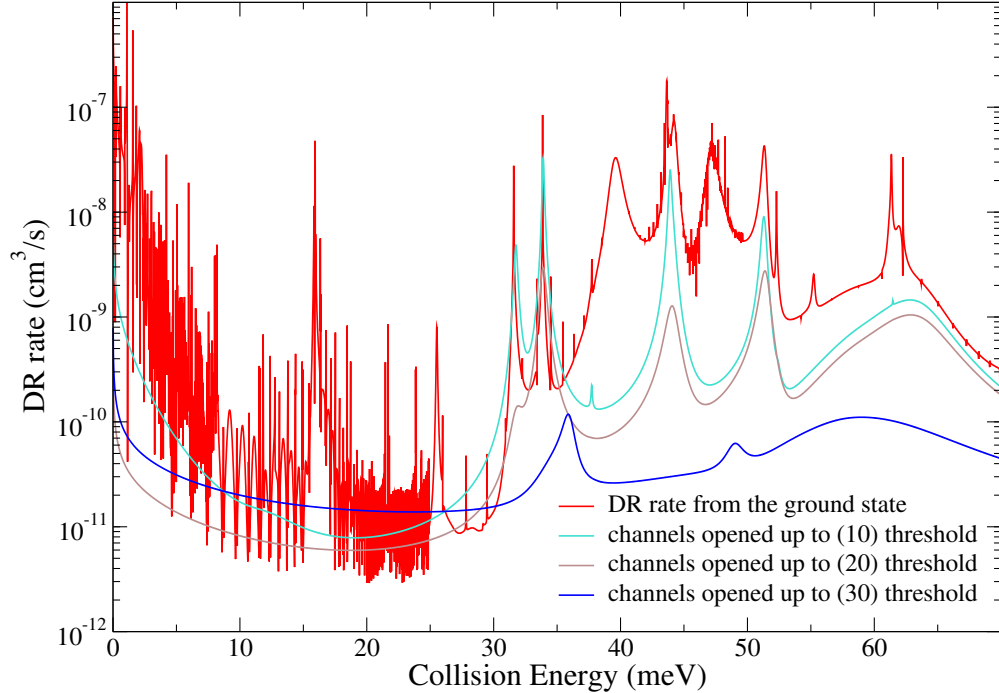


FIG. 14. The computed DR rate from the ground initial state (red curve). Other curves display calculated unphysical data in which all the closed channels are opened up to different vibrational thresholds (ν, j) (i.e., the thresholds are included in the artificial channel-opening procedure).

any dominant change in the displayed energy window when the remaining rotational thresholds (up to $(0,12)$ included in the calculations) were opened. Fig. 13 suggests that the enhancement of the DR rate around 16 meV and 40–50 meV is not caused by closed-channel resonances attached to rotationally excited states.

These results motivated a second theoretical experiment in which all the closed channels are artificially opened up to different vibrational thresholds $(\nu, 0)$. Corresponding DR rates are displayed in Fig. 14. It is quite clear that already opening the first vibrational threshold (turquoise curve) removes the resonance at 16 meV and another 2 resonances in the 40–50 meV domain. Artificial opening of the higher vibrational thresholds removes more of the resonant structure and flattens the DR rate in the examined energy window.

One can, therefore, conclude that the enhancement of the DR rate (by 2–3 orders of magnitude) at 40–50 meV is caused by overlapping of the closed-channel resonances attached to different vibrational thresholds - a behavior similar to what was previously observed for the LiH system [16, 44].

VI. CONCLUSIONS

The calculated data and insights are derived from an *ab initio* study describing inelastic collisions between low-energy electrons and the HeH^+ cation.

One of the goals of the present work has been to address how one's choice of the frame of reference affects the computed results. This important question was previously raised by Takagi and Tashiro 2015 [14], where the authors observed a difference of about 2 orders of magnitude in the DR rates when using the center-of-mass (CMS) versus the center-of-charge (CCS) frames of reference. We have not been able to confirm this conclusion, as we observe differences smaller than 30% for collision energies below 100 meV (Fig. 8). Moreover, the difference in the DR rates becomes negligible for collision energies above 100 meV. The difference is somewhat more pronounced (up to a factor of 2) in the case of the rotationally inelastic collisions, especially for the $0 \rightarrow 1$ and $0 \rightarrow 3$ transitions (left panel of Fig. 6). The strong $0 \rightarrow 2$ transition, dominated by the frame-invariant quadrupole moment of the cation, remains unchanged by the frame of reference change.

Our inelastic rates indicate that rotational excitation is a process almost two orders of magnitude more probable than vibrational excitation. Several rotational transitions are compared, after carrying out the thermal-averaging convolution, with the recent calculations of Hamilton *et al.* 2016 (right panel of Fig. 6). The agreement with the previous calculations is quite good, with notable differences for the $0 \rightarrow 1$ and $0 \rightarrow 3$ transitions. We assume that these differences are caused by the Born-closure technique applied in the previous study.

For the case of dissociative recombination, the computed data reproduce most of the structures visible in the available experiments for all the HeH^+ isotopologues (Fig. 9). Furthermore, the absolute experimental DR rate values, available for the isotopologues $^4\text{HeH}^+$ and $^3\text{HeH}^+$, agree well with the present calculations. Our further analysis of the DR mechanism has revealed that while the rotationally excited neutral high- n HeH molecules form long-lived resonant states, especially when created by below-threshold rotationally inelastic collisions of electrons with the cations, these temporary neutral states nevertheless do not contribute much to the dissociation probability.

The situation is very different for the temporary neutral high- n HeH molecules, created by below-threshold vibrationally inelastic collisions of electrons with the HeH^+ cations. These resonant states lead to dissociation with very high probability (about 90%). Since the similar behavior was observed before for the LiH^+ molecule [16], it may represent a universal mechanism common for all the indirect DR processes.

Finally, we attribute the strong DR enhancements visible below 100 meV to the overlap of

complex resonance manifolds that couple closed vibrational channels having both high and low principal quantum numbers n . These overlaps are of the same type that have been studied in molecular Rydberg spectroscopy in recent decades [46–49].

ACKNOWLEDGMENTS

RČ conducted this work within the COST Action CM1301 (CELINA) and the support of the Czech Ministry of Education (Grant No. LD14088) is acknowledged. The work of CHG is supported in part by the U.S. Department of Energy, Office of Science, under Award No. de-sc0010545. We thank O. Novotny for his encouragement to carry out this investigation.

-
- [1] W. Roberge and A. Dalgarno, *Astrophys. J.* **255**, 489 (1982).
 - [2] F. B. Yousif and J. B. A. Mitchell, *Phys. Rev. A* **40**, 4318 (1989).
 - [3] F. B. Yousifand, J. B. A. Mitchell, M. Rogelstad, A. Lepadellec, A. Canosa, and M. I. Chibisov, *Phys. Rev. A* **49**, 4610 (1994).
 - [4] G. Sundstrom, S. Datz, J. R. Mowat, S. Mannervik, L. Brostrom, M. Carlson, H. Danared, and M. Larsson, *Phys. Rev. A* **50**, R2806 (1994).
 - [5] T. Tanabe, I. Katayama, N. Inoue, K. Chida, Y. Arakaki, T. Watanabe, M. Yoshizawa, M. Saito, Y. Haruyama, K. Hosono, et al., *Phys. Rev. A* **49**, R1531 (1994).
 - [6] J. R. Mowat, H. Danared, G. Sundstrom, M. Carlson, L. H. Andersen, L. Vejbychristensen, M. af Ugglas, and M. Larsson, *Phys. Rev. Lett.* **74**, 50 (1995).
 - [7] C. Stromholm, J. Semaniak, S. Rosen, H. Danared, S. Datz, W. van der Zande, and M. Larsson, *Phys. Rev. A* **54**, 3086 (1996).
 - [8] J. Semaniak, S. Rosen, G. Sundstrom, C. Stromholm, S. Datz, H. Danared, M. af Ugglas, M. Larsson, W. J. van der Zande, Z. Amitay, et al., *Phys. Rev. A* **54**, R4617 (1996).
 - [9] T. Tanabe, I. Katayama, S. Ono, K. Chida, T. Watanabe, Y. Arakaki, Y. Haruyama, M. Saito, T. Odagiri, K. Hosono, et al., *J. Phys. B: Atom. Molec. Phys.* **31**, L297 (1998).
 - [10] S. L. Guberman, *Phys. Rev. A* **49**, R4277 (1994).
 - [11] B. K. Sarpal, J. Tennyson, and L. A. Morgan, *J. Phys. B: Atom. Molec. Phys.* **27**, 5943 (1994).
 - [12] H. Takagi, *Phys. Rev. A* **70**, 022709 (2004).
 - [13] D. J. Haxton and C. H. Greene, *Phys. Rev. A* **79**, 022701 (2009), erratum-*ibid.* **84**, 039903(E) (2011).
 - [14] H. Takagi and M. Tashiro, in *DR2013: Ninth international conference on dissociative recombination: Theory, experiment, and applications*, edited by I. Schneider, O. Dulieu, and J. Robert (2015), vol. 84 of *EPJ Web of Conferences*, p. 02002, 9th International Conference on Dissociative Recombination: Theory, Experiment, and Applications, Paris, France, Jul 07-12, 2013.

- [15] J. R. Hamilton, A. Faure, and J. Tennyson, **455**, 3281 (2016).
- [16] R. Curik and C. H. Greene, *Phys. Rev. Lett.* **98**, 173201 (2007).
- [17] R. Curik and F. A. Gianturco, *Phys. Rev. A* **87**, 012705 (2013).
- [18] R. von Hahn, A. Becker, F. Berg, K. Blaum, C. Breitenfeldt, H. Fadil, F. Fellenberger, M. Froese, S. George, J. Goeck, et al., *Rev. Sci. Instrum.* **87**, 063115 (2016).
- [19] D. Zajfman, A. Wolf, D. Schwahn, D. A. Orlov, M. Grieser, R. von Hahn, C. P. Welsch, J. R. C. Lopez-Urrutia, C. D. Schroter, X. Urbain, et al., in *DR2004: Sixth International Conference on Dissociative Recombination: Theory, Experiments and Applications*, edited by A. Wolf, L. Lammich, and P. Schmelcher (2005), vol. 4 of *J. Phys. Conf. Ser.*, pp. 296–299.
- [20] N. Moiseyev, *Phys. Rep.* **302**, 212 (1998).
- [21] L. A. Morgan, C. J. Gillan, J. Tennyson, and X. S. Chen, *J. Phys. B: Atom. Molec. Phys.* **30**, 4087 (1997).
- [22] I. Ema, J. M. G. D. la Vega, G. Ramirez, R. Lopez, J. F. Rico, H. Meissner, and J. Paldus, *J. Chem. Phys.* **24**, 859 (2003).
- [23] A. Yiannopoulou, G. H. Jeung, S. J. Park, H. S. Lee, and Y. S. Lee, *Phys. Rev. A* **59**, 1178 (1999).
- [24] S. N. Altunata and R. W. Field, *Phys. Rev. A* **67**, 022507 (2003).
- [25] M. E. Dolan and F. Masnouseeuws, *J. Phys. B: Atom. Molec. Phys.* **14**, L583 (1981).
- [26] E. de Prunelé, *Phys. Rev. A* **36**, 3015 (1987).
- [27] N. Y. Du and C. H. Greene, *Phys. Rev. A* **36**, 971 (1987), erratum-ibid. **36**, 5467(E) (1987).
- [28] C. H. Greene, A. S. Dickinson, and H. R. Sadeghpour, *Phys. Rev. Lett.* **85**, 2458 (2000).
- [29] A. S. Dickinson and F. X. Gadea, *Phys. Rev. A* **65**, 052506 (2002).
- [30] A. A. Khuskivadze, M. I. Chibisov, and I. I. Fabrikant, *Phys. Rev. A* **66**, 042709 (2002).
- [31] V. Bendkowsky, B. Butscher, J. Nipper, J. P. Shaffer, R. Loew, and T. Pfau, *Nature* **458**, 1005 (2009).
- [32] M. J. SEATON, *Rep. Prog. Phys.* **46**, 167 (1983).
- [33] E. S. Chang and U. Fano, *Phys. Rev. A* **6**, 173 (1972).
- [34] A. J. F. Siegert, *Phys. Rep.* **56**, 750 (1939).
- [35] P. A. Batishchev and O. I. Tolstikhin, *Phys. Rev. A* **75**, 062704 (2007).
- [36] D. E. Woon and T. H. Dunning, *J. Chem. Phys.* **100**, 2975 (1994).
- [37] J. A. Coxon and P. G. Hajigeorgiou, *J. Chem. Phys.* **193**, 306 (1999).
- [38] K. Pachucki and J. Komasa, *J. Chem. Phys.* **137**, 204314 (2012).
- [39] C. H. Greene and C. Jungen, *Phys. Rev. Lett.* **55**, 1066 (1985).
- [40] E. L. Hamilton and C. H. Greene, *Phys. Rev. Lett.* **89**, 263003 (2002).
- [41] M. Aymar, C. H. Greene, and E. Luc-Koenig, *Rev. Mod. Phys.* **68**, 1029 (1996).
- [42] M. A. Morrison and W. Sun, in *Computational Methods for Electron-Molecule Collisions*, edited by W. M. Hue and F. A. Gianturco (Plenum Press, New York, 1995), chap. 6, p. 170, 1st ed.
- [43] I. Rabadan and J. Tennyson, *Comput. Phys. Commun.* **114**, 129 (1998).
- [44] R. Curik and C. H. Greene, *Mol. Phys.* **105**, 1565 (2007).

- [45] V. Kokoouline and C. H. Greene, *Phys. Rev. A* **72**, 022712 (2005).
- [46] C. Jungen and D. Dill, *J. Chem. Phys.* **73**, 3338 (1980).
- [47] N. Y. Du and C. H. Greene, *J. Chem. Phys.* **85**, 5430 (1986).
- [48] G. M. Greetham, U. Hollenstein, R. Seiler, W. Ubachs, and F. Merkt, *Phys. Chem. Chem. Phys.* **5**, 2528 (2003).
- [49] F. Texier, C. Jungen, and S. C. Ross, *Faraday Disc.* **115**, 71 (2000).